Pergamon

Int. J. Heat Mass Transfer. Vol. 38, No. 17, pp. 3253–3262, 1995

0017–9310/95 $9.50 + 0.00

0017–9310(95)00056–9

Heat and mass transfer with condensation in a fibrous insulation slab bounded on one side by a cold surface

KEIJI MURATA

Research Laboratory I, Energy and Mechanical Research Laboratories, Research and Development Center, Toshiba Corporation, 4-1, Ukishima-cho, Kawasaki-ku, Kawasaki 210, Japan

(*Received* 14 *July* 1994 *and in final form* 9 *January* 1995)

Abstract—This work presents an experimental and analytical investigation of heat and mass transfer with condensation in a fibrous insulation slab, one side of which is exposed to high temperature and high humidity, and the other side bounded by a cold surface. The analysis carried out is based on a model in which condensation occurs on the cold surface and in the interior of the fibrous insulation, and condensate falls away under gravity. Predicted heat transfer coefficients agreed well with experimental data at atmospheric pressure and temperatures up to 100°C. It was also indicated by the analysis that the convective contribution is appreciable in higher pressure and temperature environments.

1. INTRODUCTION

Many investigations on heat and mass transfer with phase changes in porous media have been performed, with the aim of applying the results to geothermal engineering, drying technology, nuclear waste disposal, and so on [1–3]. Since about 1980, the effect of condensation on the performance of highly porous insulation materials has become an important topic in the area of energy conservation. Some studies [4–7] on condensation in a porous slab exposed to different humidity levels on two faces have been reported. According to these studies, the process of condensation in an initially dry porous slab takes place in three stages as follows. Firstly, velocity, temperature and vapor concentration fields develop within the porous slab, and condensation begins. However, the quantity of condensate is very small at this stage, and it accumulates mostly in a bound form. This stage is relatively short compared with the others. In the second stage, although the liquid content increases gradually, it is still so small that the condensate remains pendular, and does not move. Furthermore, since the liquid content is still small enough to have little effect on various properties, the local velocity, temperature, vapor concentration and condensation rate remain almost invariable in time. When the liquid content increases further and goes beyond a certain critical value, the pendular drops of condensate coalesce and begin to move under surface tension and gravity. Ultimately, a steady state is attained and the liquid content, as well as the velocity, temperature, vapor concentration and condensation rate, becomes constant. The local liquid content is controlled by the balance between the condensation rate and the liquid flux.

Ogniewicz and Tien [4] and Vafai and Sarkar [5] analysed heat and mass transfer in the second stage, where the condensate remains immobile. Ogniewicz and Tien [4] assumed that the properties of the gas phase were constant and equal to those of dry gas, while Vafai and Sarkar [5] took the change in gas density into account. Analysis of the final stage, where the condensate becomes mobile, has been performed by Motakef and El-Masri [6], and Shapiro and Motakef [7]. Both of these analyses assumed that condensate moved under surface tension forces and that the liquid flux was proportional to the liquid content gradient. On the other hand, convective contributions were neglected.

In chemical reactors and similar equipments, fibrous insulation slabs are often fitted inside the walls in order to protect them from the high-temperature gas and to reduce heat losses. In such cases, there exists a situation in which one side of the fibrous insulation slab is exposed to a high-temperature, high-humidity environment, while the opposite face is bounded by a cold surface. This paper reports an experimental and analytical investigation of condensation phenomena in such a fibrous insulation slab. The analysis is based on a model in which condensation occurs on the cold surface and in the interior of the fibrous insulation, and condensate is assumed to fall under gravity. In a high-pressure, high-temperature and high-humidity environment, the change in properties (thermal conductivity, density and so on) within the insulation is expected to be significant enough to have effects on the velocity, temperature and vapor concentration fields. Furthermore, the convective contribution is often appreciable. Thus, this was taken into account in the analysis, and some calculations were also carried out under conditions of

NOMENCLATURE

b	width of air flow channel [m]
C_p	specific heat of gas phase [J kg^{-1} K^{-1}]
D_G	diffusion coefficient of gas phase [m^2 s^{-1}]
d	thickness of fibrous insulation slab [m]
g	gravitational acceleration, $\simeq$9.81 [m s^{-2}]
h_{fg}	latent heat of condensation [J kg^{-1}]
i	x-direction mesh number
J, j	y-direction mesh number
K	permeability [m^2]
M	molecular weight
m	mesh number at the boundary between dry and wet zones
n	maximum mesh number in x direction
P	pressure [Pa] or [MPa]
P_0	pressure at $y = 0$ [Pa] or [MPa]
P_g	partial pressure of noncondensable gas [Pa] or [MPa]
P_S	saturation vapor pressure of water [Pa] or [MPa]
P_v	partial pressure of water vapor [Pa] or [MPa]
q	heat flux through the cooling surface [W m^{-2}]
q_{LH}	heat flux due to latent heat of condensation [W m^{-2}]
R	gas constant [J kmol^{-1} K^{-1}]
T	temperature [°C] or [K]
T_S	saturation temperature corresponding to the local vapor concentration [°C] or [K]
t	elapsed time after the start of humidification [s]
u	x-direction velocity [m s^{-1}]
v	y-direction velocity [m s^{-1}]
v_{ch}	air velocity in the air flow channel [m s^{-1}]
w	mass fraction of vapor in gas phase
x	x coordinate [m]
x_b	x coordinate at the boundary between dry and wet zones [m]
Δx	x-direction mesh width [m]
y	y coordinate [m]
Δy	y-direction mesh width [m].

Greek symbols

α	heat transfer coefficient [W m^{-2} K^{-1}]
Γ	volumetric condensation rate [kg m^{-3} s^{-1}]
δ_{LF}	liquid film thickness [m]
$\delta_{LF,cr}$	critical liquid film thickness [m]
ε	volume fraction
η	viscosity [kg m^{-1} s^{-1}]
λ	thermal conductivity [W m^{-1} K^{-1}]
ξ	function of the topology of the liquid phase in reference [1]
ρ	density [kg m^{-3}].

Subscripts

1	at the location $y = 30$ mm
2	at the location $y = 70$ mm
g	non-condensable gas, namely air
DZ	dry zone
e	equivalent
G	gas phase
i	gas–liquid interface of liquid film
J	at $j = J$
IN	inlet of air flow channel
L	liquid phase
LF	falling liquid film
S	solid or saturation
v	water vapor
W	cooling surface
WZ	wet zone
0	at the surface ($x = 0$) or at the top ($y = 0$) of the fibrous insulation slab.

higher pressure and higher temperature, although the experiments were conducted at atmospheric pressure and temperatures up to 100°C. It is known that radiative heat transfer is important at high temperature [8, 9]. However, this study is confined to heat and mass transfer accompanied by condensation, and the radiative contribution is not mentioned.

2. EXPERIMENTS

2.1. *Experimental apparatus*

Figure 1(a) and (b) is a schematic diagram of the experimental apparatus and a cross section of the test section, respectively. The experimental apparatus consists of a blower, a strainer, a float-type flowmeter, a measuring chamber, a pre-heater, a humidifier, mixing channels, a main heater, a test section and a cooler. First, air is rid of dust and moisture at the strainer. The flow rate of the air is measured by the flowmeter. The initial temperature and humidity are measured by the 0.5 mm diameter copper–constantan thermocouple and hygrometer at the measuring chamber, respectively. After being heated to above dew point in the pre-heater, the air is humidified to the desired vapor concentration in the humidifier. A fixed quantity of distilled water is supplied to the humidifier by a volumetric feed pump, and evaporates from a copper block heated by an electric heater. Although the volumetric feed pump is of the intermittent type, fluctuations in vaporization rate are suppressed by keeping a porous medium on the copper block wet. The wet air (namely, the mixture of air and water vapor)

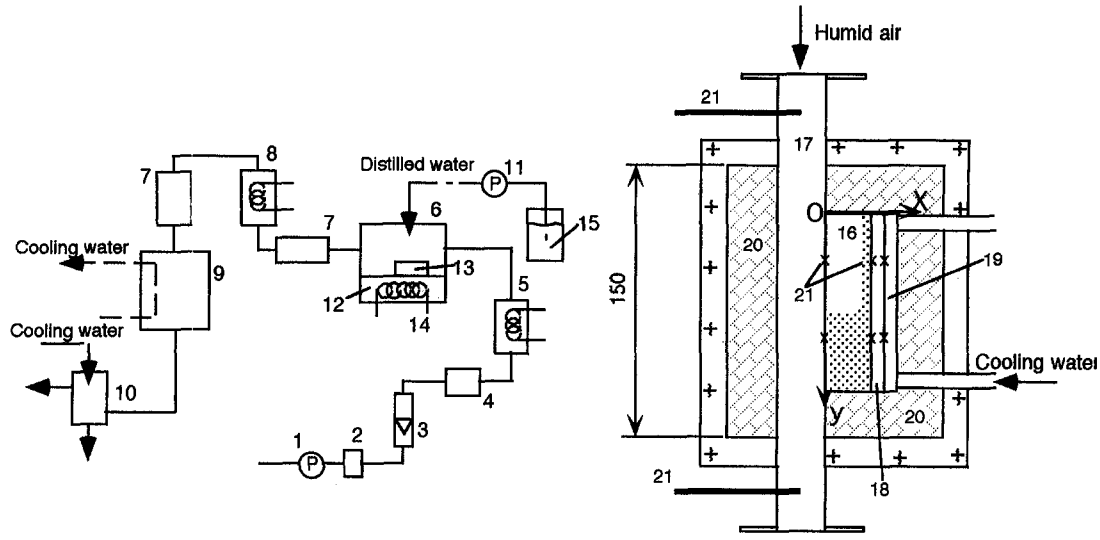

1 Blower
2 Strainer
3 Flowmeter
4 Measuring chamber
5 Pre-heater
6 Humidifier
7 Mixing channel
8 Main heater
9 Test section
10 Cooler
11 Volumetric feed pump
12 Copper block
13 Fibrous porous medium
14 Electric heater
15 Distilled water
16 Test piece
17 Air flow channel
18 Glass plate
19 Cooling panel
20 Insulation wall
21 Thermocouple

Fig. 1. Experimental apparatus: (a) schematic diagram; (b) test section.

flowing out of the humidifier is heated to a desired temperature by the main heater, and flows through the mixing channels into the test section. Twisted tapes are placed in the mixing channels to ensure adequate mixing. The wet air flowing out of the test section is cooled and dried in the cooler, and then discharged into the atmosphere. The main components and channels of the apparatus are heated to above dew point by micro-heaters, and are thermally insulated with fibrous insulation.

The test section comprises a test piece, an air flow channel, a glass plate, a cooling panel and insulating walls. The test piece is a fibrous insulation slab made of Al_2O_3(46%) and SiO_2(54%), and its porosity is 0.962. It is 100 mm deep, 100 mm wide and 25 mm thick. One side of the test piece (100 × 100 mm) is bounded by the glass plate, and the opposite side forms a part of the air-flow channel. An adhesive agent is applied to the other four sides (100 × 25 mm) so that wet air and condensate cannot permeate through them. Wet air temperatures are measured using 0.5 mm diameter copper–constantan thermocouples at the inlet and outlet of the air-flow channel. The glass plate is 8 mm thick, and is attached to a panel cooled by water. Surface temperatures of the test piece and the glass plate are measured by 0.25 mm diameter chromel–alumel thermocouples. The measuring points indicated by the × symbols in Fig. 1(b) are at two levels (the distance from the top, $y = 30$ mm and $y = 70$ mm) in the center of the test piece. The heat flux at each location, q, was obtained from the thermal conductivity and the surface temperature difference of the glass plate. Vapor concentration in the wet air was estimated from the air flow rate, the initial humidity measured at the measuring chamber, and the flow of water supplied to the humidifier.

2.2. *Experimental procedure*

First, air adjusted to a fixed temperature is supplied to the test section without humidification, and the test piece and insulation walls are heated to a prescribed temperature. At the same time, the cooling panel is cooled by water. Care must be taken to ensure that the surface temperature of the glass plate does not fall below the dew temperature. After enough time for establishing a steady state has elapsed, air humidification is begun by supplying distilled water to the humidifier. Changes in wet air temperature T_{IN}, surface temperatures of the test piece T_{01} and T_{02}, cooling surface temperature T_w (the surface temperature of the glass plate) and heat flux q are measured. Measurements are carried out at intervals of about 30 s for 8 or 9 h.

Before the main experiments, preliminary tests were

Table 1. Experimental conditions

	W_0	T_{S0} (°C)	T_0 (°C)	T_w (°C)	$T_{S0}-T_w$ (K)
Run 1	0.35	79.8	89	24	55.8
Run 2	0.35	79.8	89	50	29.8
Run 3	0.35	79.8	89	62	17.8
Run 4	0.20	68.4	89	34	34.4
Run 5	0.20	68.4	89	50	18.4

conducted without humidification. In these preliminary experiments, the dependence of heat flux q on the air velocity in the air flow channel v_{ch} and the width of the air-flow channel b were examined. The experimental conditions were (1) $b = 5$ mm, $v_{ch} = 1.0$ m s^{-1}, (2) $b = 5$ mm, $v_{ch} = 0.53$ m s^{-1} and (3) $b = 30$ mm, $v_{ch} = 0.17$ m s^{-1} at $T_0 = 89$°C and $T_w = 30$°C. Since the difference in q under these three conditions was small, the width of the air-flow channel b was fixed at 5 mm for the main experiments. (In Fig. 1(b), however, the air flow channel is drawn as 30 mm in width.) In the main experiments, the conditions were as follows: air pressure $P_0 = 0.10$ MPa (atmospheric pressure); surface temperature of the test piece $T_0 = 89$°C; cooling surface temperature $T_w = 24$–62°C; vapor concentration in wet air (the mass fraction of vapor) $w_{IN} = 0.35$ and 0.20. The mole fractions corresponding to $w_{IN} = 0.35$ and 0.20 are 0.464 and 0.287, and the dew temperatures are 79.8°C and 68.4°C, respectively. The air velocity in the air-flow channel, v_{ch}, was about 1.0 m s^{-1}, and the temperature decrease of wet air in the air-flow channel was smaller than 3 K. The decrease in vapor concentration was estimated to be smaller than 3% at the location $y = 70$ mm. The vapor concentration at the surface of the test piece, w_0, is regarded to be almost equal to that at the inlet of the test section w_{IN}, and w_0 is used instead of w_{IN} hereafter. The conditions for all experimental runs are shown in Table 1.

2.3. *Experimental results and discussion*

The experimental results for Run 1 and Run 5 are shown, respectively, in Fig. 2(a) and (b), where the horizontal axis is the elapsed time after the start of humidification, t. T_{IN} is the air temperature at the inlet of the test section, and T_{S0} is the dew temperature corresponding to the vapor concentration, w_0. Subscripts 1 and 2 denote the two measuring positions at $y = 30$ mm and $y = 70$ mm respectively. The cooling surface temperature, T_w, is shown only for $y = 30$ mm as it was almost independent of measuring position. A steady state was established before the start of humidification ($t \leqslant 0$). The symbols ○, ◇, □, △ and ▽ on the vertical axis denote T_{IN}, T_{01}, T_w, q_1 and q_2 at $t = 0$.

In Run 1, although T_{01}, T_{02} and T_{IN} went up sharply just after the start of humidification, T_{01} and T_{02} then reached the target temperature (=89°C) about 30 min later as T_{IN} was adjusted, and remained almost

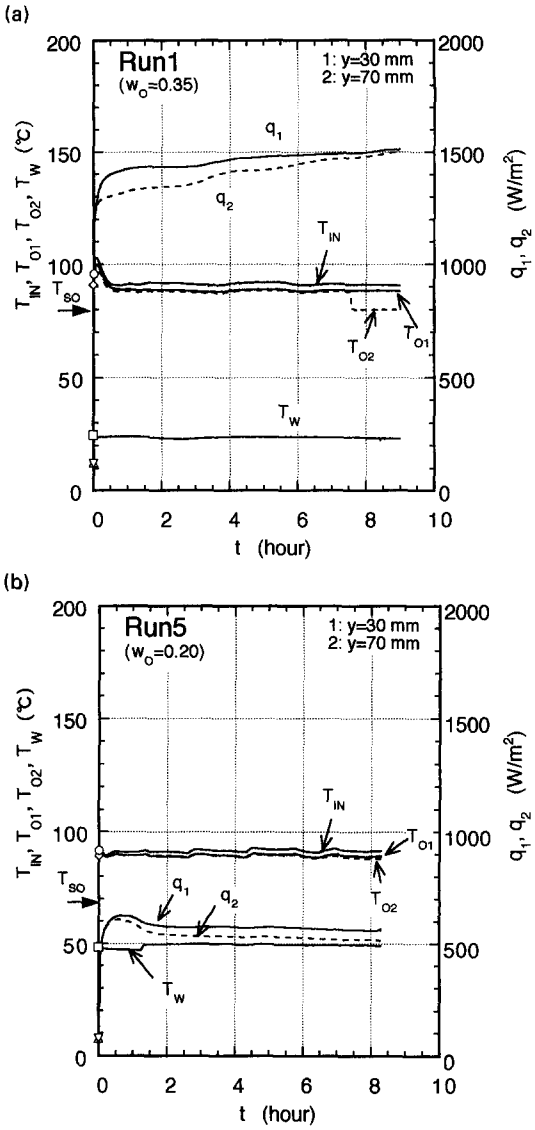

Fig. 2. (a) Changes in q_1, q_2, T_{IN}, T_{01}, T_{02} and T_w for Run 1 (○ : T_{IN}, ◇ : T_{01}, □ : T_w, △ : q_1, ▽ : q_2 at $t = 0$). (b) Changes of q_1, q_2, T_{IN}, T_{01}, T_{02} and T_w for Run 5 (○ : T_{IN}, ◇ : T_{01}, □ : T_w, △ : q_1, ▽ : q_2 at $t = 0$).

invariable after that. However, T_{02} dropped to about 80°C abruptly at around $t = 7.5$ h. According to observations of the test piece made just after the end of the experimental run, an extensive region at the bottom was full of condensate, as indicated by the dotted region in Fig. 1(b) (about $y = 60$–100 mm), while only in the vicinity of the cooling surface was the material wet with condensate towards the top (about $y = 0$–60 mm). Thus, it is verified that condensation occurs in the vicinity of the cooling surface, and that the condensate falls under gravity with little influence of capillary action. Furthermore, it seems that the abrupt drop in T_{02} was caused by an accumulation of condensate at the bottom of the test piece. This explanation is consistent with the fact that the T_{02} value after the sudden fall in temperature was almost

equal to the dew temperature (=79.8°C). Such an abrupt drop in T_{02} was not observed in other experimental runs where the condensation rate was relatively small. Heat flux q_1 went up rapidly just after humidification began, becoming almost invariable around $t = 1$ h. However, it began to increase gradually after $t = 4$ h. Heat flux q_2 did not change noticeably until $t = 2$ h, but increased gradually after that. It seems that these gradual increases in q_1 and q_2 were the result of an accumulation of condensate at the bottom of the test piece.

We next consider the results obtained for Run 5. Heat fluxes q_1 and q_2 overshot just after humidification began, becoming invariable at approximately $t = 2$ h. Such overshoot by q_1 and q_2 arose because the cooling surface temperature, T_w, was about 3 K lower than the target (=50°C) during the first 1.5 h. On the other hand, although T_{01} and T_{02} sometimes changed in response to T_{IN}, q_1 and q_2 were hardly affected. Thus, q depends on w_0 and T_w much more than on T_0. This implies that the driving force of condensation is not the temperature difference $T_0 - T_w$, but rather the vapor concentration difference $w_0 - w_w$, or the difference in saturation temperature, $T_{S0} - T_w$.

Figure 3 shows the heat transfer coefficient α at a steady state versus $T_{S0} - T_w$, where α is defined by

$$\alpha = \frac{q}{T_{S0} - T_w}. \tag{1}$$

On the basis of the above understanding of Run 1, the α values at $t = 2$ h are taken as the steady-state data for Run 1.

The uncertainty in the α value is caused by uncertainties in the thermal conductivity (5%) and the surface temperature difference (0.3 K) of the glass plate, and the temperature difference, $T_{S0} - T_w$ (1.0 K).

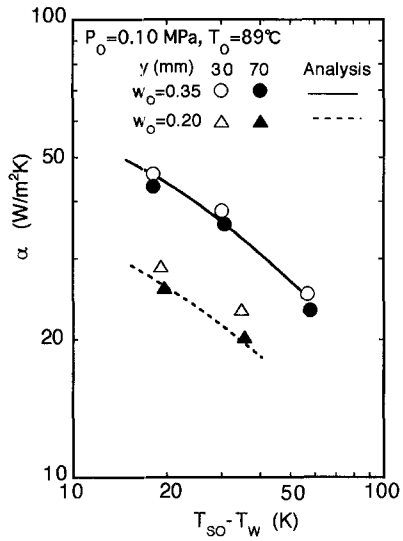

Fig. 3. Comparison between experimental and analytical results.

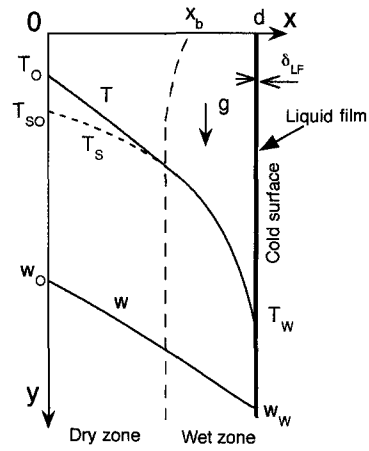

Fig. 4. Analytical model and coordinates.

From these uncertainties, the uncertainty in the α data was estimated to be within $\pm 10\%$.

The solid and broken lines are the predicted values of α using the analysis described later. The heat transfer coefficient α goes down with decreasing w_0 and increasing $T_{S0} - T_w$. Detailed discussions will be presented later.

3. ANALYSIS

3.1. *Mathematical formulation*

A heat and mass transfer model of a fibrous insulation slab and the coordinates used are shown in Fig. 4. One side of the fibrous insulation slab is exposed to a high-temperature and high-humidity environment at $x = 0$, where the temperature and the vapor concentration are kept at T_0 and w_0 respectively. The opposite side is bounded by a vertical cooling surface at $x = d$. When the cooling surface temperature T_w is kept below the dew temperature, T_{S0}, condensation of vapor can be expected to occur at the cooling surface and in the interior of the insulation. As indicated in Fig. 4, the insulation slab can be divided into the following three regions: the dry zone, where no liquid phase is found; the wet zone, where solid (fiber), gas, and liquid phases coexist; and the liquid-film zone, where condensate condensing on the cooling surface falls down and there is no gas phase. Although the wet zone is not always present, the dry zone exists as long as the gas phase is not saturated at the surface of the fibrous insulation slab ($T_0 > T_{S0}$). Heat and mass transfer in the dry and wet zones are solved for the steady state; namely, for the third stage of the condensation process as described before. The heat transfer resistance of the liquid film zone is so small that it is not solved in detail, but rather is included as a boundary condition.

The main assumptions and restrictions are as follows:

1. The fibrous insulation slab is homogeneous and isotropic.

2. The gas phase is continuous, and regarded as an ideal gas.
3. Local thermal equilibrium exists among all phases.
4. Capillary pressure is negligible compared with the partial pressure of vapor.
5. Darcy's law is valid for gas and liquid flows.
6. Capillary action has a negligible effect on liquid flow. This assumption was confirmed to be reasonable through experiments.
7. A boundary-layer approximation is valid.
8. The sensible heat transferred by liquid flow is negligible.
9. The liquid film is so thin compared with the fibrous insulation slab that the changes in dry- and wet-zone widths due to an increase in liquid-film thickness is negligible.
10. The gas density is negligible compared with the liquid density.

The governing equations for heat and mass transfer are based on Whitaker's work [1].

Energy equation:

$$\frac{\partial}{\partial x}(\rho_G C_{pG} u_G T)+\frac{\partial}{\partial y}(\rho_G C_{pG} v_G T) - \frac{\partial}{\partial x}\left[\lambda_e \frac{\partial T}{\partial x}\right] = h_{fg}\Gamma \quad (2a)$$

$$\lambda_e = \varepsilon_S \lambda_S + \varepsilon_G \lambda_G + \varepsilon_L \lambda_L. \quad (2b)$$

Gas phase continuity equation:

$$\frac{\partial}{\partial x}(\rho_G u_G)+\frac{\partial}{\partial y}(\rho_G v_G)+\Gamma = 0. \quad (3)$$

Gas phase momentum equation (Darcy's law):

$$u_G = -\frac{K_G \varepsilon_G}{\eta_G}\frac{\partial P}{\partial x} \quad (4)$$

$$v_G = -\frac{K_G \varepsilon_G}{\eta_G}\left(\frac{\partial P}{\partial y}-\rho_G g\right). \quad (5)$$

Gas phase diffusion equation:

$$\frac{\partial}{\partial x}(\rho_G u_G w)+\frac{\partial}{\partial y}(\rho_G v_G w) - \frac{\partial}{\partial x}\left[\rho_G D_e \frac{\partial w}{\partial x}\right] = -\Gamma \quad (6a)$$

$$D_e = \varepsilon_G D_G. \quad (6b)$$

Liquid-phase continuity equation:

$$\frac{\partial v_L}{\partial y} = \frac{\Gamma}{\rho_L}. \quad (7)$$

Liquid-phase momentum equation (Darcy's law):

$$v_L = \frac{K_L \varepsilon_L \xi}{\eta_L}\rho_L g \quad (8)$$

where ξ is a function of the topology of the liquid phase, and $0 \leqslant \xi \leqslant 1$ [1].

Volumetric constraint:

$$\varepsilon_G+\varepsilon_L+\varepsilon_S = 1. \quad (9)$$

Thermodynamic relations:

$$P_v = P_S(T). \quad (10)$$

Equation (10) is valid in the wet zone and at the gas–liquid interface of the liquid film.

$$P_v = \rho_v R_v T \quad (11a)$$

$$R_v = R/M_v \quad (11b)$$

$$P_g = \rho_g R_g T \quad (12a)$$

$$R_g = R/M_g \quad (12b)$$

$$\rho_G = \rho_v+\rho_g \quad (13)$$

$$P = P_v+P_g \quad (14)$$

$$w = \rho_v/\rho_G. \quad (15)$$

The following equation is obtained by differentiating equations (4) and (5) with respect to y and x respectively, and then subtracting them

$$\frac{\partial u_G}{\partial y}-\frac{\partial v_G}{\partial x} = \frac{K_G}{\eta_G}\left[-\frac{\partial \varepsilon_G}{\partial y}\frac{\partial P}{\partial x} + \frac{\partial \varepsilon_G}{\partial x}\frac{\partial P}{\partial y}-\frac{\partial}{\partial x}(\rho_G \varepsilon_G g)\right]. \quad (16)$$

Omitting the first term on each side of equation (16), and then integrating it, one obtains

$$v_G = \frac{K_G}{\eta_G}(\rho_G-\rho_{G0})\varepsilon_G g. \quad (17)$$

In this analysis, the pressure P is approximated by $P = P_0+\rho_{G0} g y$. Namely, the pressure change in the x direction is neglected, and the momentum equations are not solved for pressure.

The boundary conditions are as follows.

At $x = 0$, or at the surface of the insulation slab:

$$w = w_0 \quad (18)$$

$$T = T_0. \quad (19)$$

At $x = d-\delta_{LF}$, or at the interface of the liquid film:

$$(\rho_G u_G)_i-\left(\rho_G u_G w-\rho_G D_e \frac{\partial w}{\partial x}\right)_i = 0 \quad (20)$$

$$q = (\rho_G u_G)_i h_{fg}-\left(\lambda_e \frac{\partial T}{\partial x}\right)_i = \frac{\lambda_{LF}}{\delta_{LF}}(T_i-T_w) \quad (21a)$$

$$\lambda_{LF} = \varepsilon_S \lambda_S+(1-\varepsilon_S)\lambda_L. \quad (21b)$$

The mass balance equation in the liquid film is simplified to

$$\frac{d}{dy}(\rho_L v_{LF}\delta_{LF}) = (\rho_G u_G)_i \quad (22a)$$

$$v_{LF} = \frac{K_L(1-\varepsilon_S)}{\eta_L}\rho_L g. \quad (22b)$$

At $y = 0$, or at the top of the insulation slab:

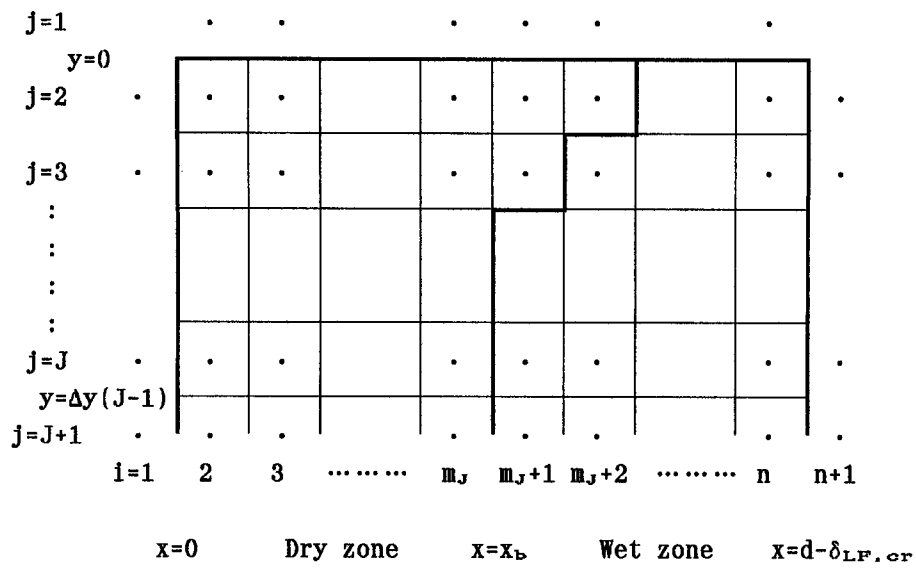

Fig. 5. Calculation scheme.

$$v_G = 0 \tag{23}$$

$$v_L = 0 \tag{24}$$

$$\delta_{LF} = \delta_{LF,cr} \tag{25}$$

where $\delta_{LF,cr}$ is the critical film thickness representing that condensate thicker than this critical value begins to precipitate.

The above equations (2)–(15) and (17) are solved in the wet zone. In the dry zone, however, ε_L, v_L and Γ are already known ($\varepsilon_L = 0, v_L = 0, \Gamma = 0$), so equations (7), (8) and (10) are not necessary. Equations (26) and (27) are based on the continuity of heat flux and diffusive flux at the boundary between wet and dry zones ($x = x_b$) respectively

$$-\left(\lambda_e \frac{\partial T}{\partial x}\right)_{wz} = -\left(\lambda_e \frac{\partial T}{\partial x}\right)_{DZ} \tag{26}$$

$$-\left(\rho_G D_e \frac{\partial w}{\partial x}\right)_{wz} = -\left(\rho_G D_e \frac{\partial w}{\partial x}\right)_{DZ}. \tag{27}$$

The position x_b is determined so that both these equations are satisfied.

3.2. *Solution procedure*

Solutions were obtained numerically based on the finite-difference method. Figure 5 shows the calculation scheme where, as described before, the width of the dry and wet zones is regarded as constant ($=d-\delta_{LF,cr}$) and they are divided into $n-1$ mesh points. The variables were defined on a staggered grid system; the scalar variables were defined at the center of each control volume, while the velocity components were defined at its surface. The convective and diffusive terms were discretized by donor-cell differencing and second-order centered differencing, respectively. In the problem studied here, the state at a certain y coordinate is affected by the upstream conditions, but not by those downstream. Accordingly, the variables at $j = J$ are obtained from those at $j = J-1$, and the same solution procedure is repeated until the final j. The boundary location between dry and wet zones at $j = J$, $x_b(J)$, and the variables at $j = J$, $u_G(i,J)$, $v_G(i,J)$, $T(i,J)$, $w(i,J)$, $\rho_G(i,J)$, $\Gamma(i,J)$, $v_L(i,J)$, $\varepsilon_L(i,J)$, $\varepsilon_G(i,J)$ and $\delta_{LF}(J)$ for $i = 1-n+1$ are obtained using the following procedure:

1. Estimate the location of the boundary between dry and wet zones, m_J.
2. Solve the governing equations without equation (26), and obtain the variables in each zone.
3. Calculate each term in equation (26) using T and ε_L obtained above, and evaluate the error which is given by

$$E = \left| \frac{\left(\lambda_e \frac{\partial T}{\partial x}\right)_{WZ} - \left(\lambda_e \frac{\partial T}{\partial x}\right)_{DZ}}{\left(\lambda_e \frac{\partial T}{\partial x}\right)_{DZ}} \right| \tag{28}$$

4. Find the m_J value which minimizes the error by repeating steps 1 through 3.
5. Repeat steps 1 through 4 with a larger n, unless the minimal error obtained in step 4 is within the tolerance ($= 10^{-3}$).

The boundary between dry and wet zones, $x_b(J)$, is regarded as $x_b = (m_J - 1)\Delta x$ with an uncertainty of one mesh width ($= \Delta x$).

3.3. *Analytical results and discussion*

Calculation conditions were chosen so as to simulate the experiments described above: pressure $P_0 = 0.10$ MPa; surface temperature of the insulation

slab $T_0 = 89°C$; cooling surface temperature $T_w = 15$–$65°C$; vapor concentration at the surface of the insulation slab $w_0 = 0.35$ and 0.20; and thickness of the insulation slab $d = 25$ mm. The gas phase was regarded as a binary mixture of air and water vapor. The gas-phase diffusion coefficient, D_G, was evaluated as a function of temperature and pressure, but the other properties ($C_{PG}, h_{fg}, \lambda_G, \lambda_L, \lambda_S, \rho_L, \eta_L, \eta_G$) were approximated by representative values obtained using the prediction methods of Reid and Sherwood [10]. The permeabilities of the gas and liquid phases, K_G and K_L, were measured beforehand, and $K_G = K_L = 1.5 \times 10^{-10}$ m^2. The factor ξ was assumed to be 0.1. The critical film thickness, $\delta_{LF,cr}$, was approximately regarded as equivalent to the surface roughness of the cooling surface, and fixed at 10 μm.

Figures 6(a) and 6(b) show the x-directional profiles of T, w, ε_L and T_S at $y = 30$ mm, where T_S is the local saturation temperature corresponding to local vapor concentration w. The conditions of the calculations in Fig. 6(a) and (b) simulate Run 1 and Run 5, respectively. The liquid film at $y = 30$ mm is very thin, with $\delta_{LF} = \delta_{LF,cr} + 7.5$ μm for Run 1 and $\delta_{LF} = \delta_{LF,cr} + 2.3$ μm for Run 5. In Run 1, condensation occurs in the range up to about 10 mm from the cooling surface. This region is the wet zone, where $T = T_S$ and $\varepsilon_L > 0$. The region where $T > T_S$ and $\varepsilon_L = 0$ is the dry zone. In Run 5, there is no wet zone, and condensation occurs only on the cooling surface. The liquid content in the wet zone, ε_L, depends on the factor ξ because ε_L is determined by the balance between local condensation rate and liquid flux. However, ε_L is so small that the local condensation rate Γ is hardly affected by it. The local concentration w decreases in the x direction. As a result, the temperature in the region where condensation occurs is considerably lower than the dew temperature at the surface of the insulation slab, T_{S0}. This shows that condensation is controlled mainly by diffusion resistance within the fibrous insulation. Although the temperature profile is approximately parabolic in the wet zone due to condensation, it is almost linear in the dry zone. Thus, the convective contribution is found to be small. On the other hand, the change in vapor concentration w is almost linear in both zones. This is because the x-directional change in ρ_G counterbalances that of w, and because the local condensation rate, Γ, is small enough to have no significant effect on the concentration profile in the wet zone (this is a result of the large latent heat of condensation). However, if the change in w for Run 1 is carefully observed, the w profile is seen to be slightly upwardly convex in the dry zone, and downwardly convex in the wet zone. The heat fluxes at the cooling surface are 1410 W m^{-2} for Run 1 and 498 W m^{-2} for Run 5, and are about 12 times larger than the values predicted from the equivalent thermal conductivity ($= \lambda_e(T_0 - T_w)/d$). In Run 1, the heat flux released by condensation on the cooling surface accounts for about 60% of the total heat flux. The calculation results at $y = 70$ mm, namely the value of q and the profiles of w and T, were almost the same as those at $y = 30$ mm, except for the liquid film thickness, δ_{LF}, and the liquid content in the wet zone, ε_L. This is because δ_{LF} and ε_L are small enough to have no significant effects on the velocity, temperature and vapor concentration fields, and the natural convective contribution is not appreciable.

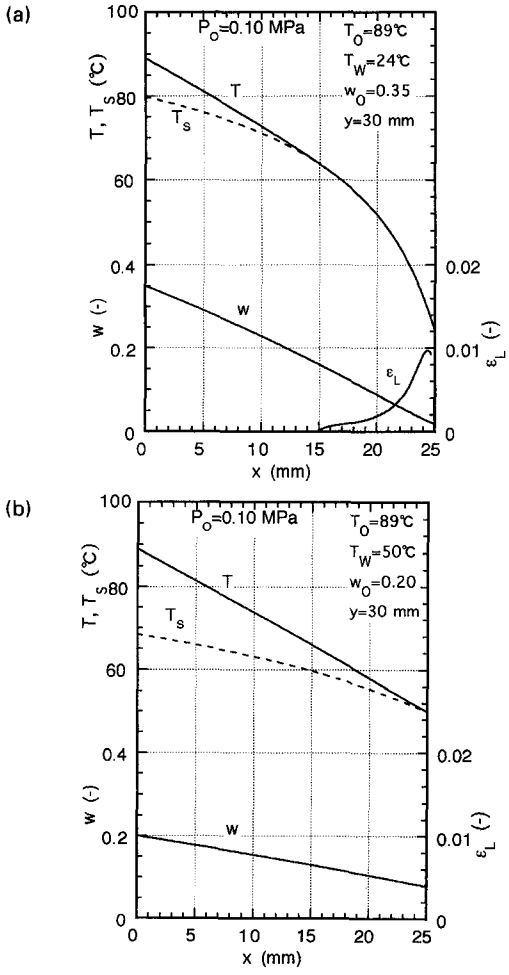

Fig. 6. (a) Profiles of T, T_S, w and ε_L for Run 1. (b) Profiles of T, T_S, w and ε_L for Run 5.

A comparison between the experimental and analytical results is given in Fig. 3, where the solid and broken lines show the two curves of predicted heat transfer coefficients, α. As the predicted α at $y = 70$ mm is almost equal to that at $y = 30$ mm, it is not shown in the figure. On the other hand, the experimental α at $y = 70$ mm is 7–12% smaller than that at $y = 30$ mm. This seems to be mainly because a vapor concentration field in the air-flow channel develops in the flow direction, and the mass transfer resistance in the air-flow channel increases (and as a result, w_0 decreases). A further reason might be that the vapor concentration in the air-flow channel decreases because of condensation within the test piece. What-

ever the reason for this small discrepancy, it is clear that the analytical and experimental results agree well although the predicted α is 10–15% lower than the experimental data at $w_0 = 0.20$.

The heat transfer coefficient α goes down with increasing $T_{S0} - T_w$. The reason for this will now be discussed. Since the condensation rate is controlled mainly by diffusion within the fibrous insulation, the heat flux, q, depends greatly on the vapor concentration difference $w_0 - w_w$, and goes up with rising saturation temperature difference $T_{S0} - T_w$. In this work, however, $T_{S0} - T_w$ is increased by reducing T_w at a fixed T_{S0}, so $w_0 - w_w$ increases less significantly at the lower T_w even if $T_{S0} - T_w$ does increase. As a result, the heat transfer coefficient, α, apparently decreases with increasing $T_{S0} - T_w$. This is because dependence of the saturation vapor pressure on the temperature becomes less significant as the temperature approaches 0°C.

The reason why the heat transfer coefficient α goes down with decreasing w_0 at a fixed $T_{S0} - T_w$ is also explained in the same way. The dependence of the saturation vapor pressure on the temperature becomes less significant at lower temperature. Accordingly, $w_0 - w_w$ for $w_0 = 0.20$ ($T_{S0} = 68.4$°C) is smaller than that for $w_0 = 0.35$ ($T_{S0} = 79.8$°C) even when $T_{S0} - T_w$ is equal.

Although the natural convective contribution is small under the experimental conditions adopted here, it is expected to become appreciable at higher pressures (where the gas density is greater), greater temperature differences and smaller condensation rates. Figures 7(a) and 7(b) show the calculation results for the condition of $P_0 = 0.81$ MPa, $T_0 = 800$°C, $T_w = 80$°C, $w_0 = 0.20$ and $d = 200$ mm. Figure 7(a) shows the y-directional changes in q and q_{LH}, where q_{LH} is the heat flux due to the latent heat of condensation. Figure 7(b) shows the temperature profiles at various y coordinates. In these calculations, λ_G and η_G were also evaluated as a function of temperature. The radiative contribution was not taken into account, although it might be expected to be appreciable at such a high temperature. No wet zone exists under this condition. The heat flux and the temperature profile change significantly in the y direction: this is a result of natural convection.

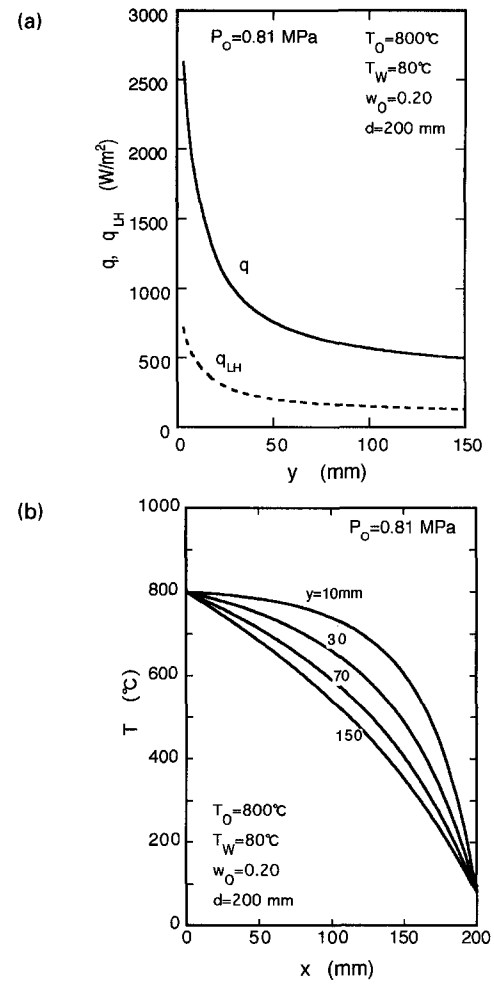

Fig. 7. (a) Changes in q and q_{LH} in the y direction. (b) Temperature profiles in a fibrous insulation slab.

4. CONCLUDING REMARKS

Condensation in a fibrous insulation slab, one side of which is exposed to a high-temperature and high-humidity environment, while the other side is bounded by a cold surface, has been investigated experimentally and analytically. The analysis was based on a model in which condensation occurs on the cold surface and in the interior of the insulation, and condensate flows under gravity but not by capillary action. The predicted heat transfer coefficients agreed well with the experimental data at atmospheric pressure and for temperatures up to 100°C. It was also indicated by the analysis that the convective contribution is appreciable at higher pressures and temperatures.

REFERENCES

1. S. Whitaker, Simultaneous heat, mass and momentum transfer in porous media: a theory of drying, *Advances in Heat Transfer* Vol. 13, pp. 119–203. Academic Press, New York (1977).
2. E. R. G. Eckert and E. Pfender, Heat and mass transfer in porous media with phase change, *Proceedings of the Sixth International Heat Transfer Conference*, Vol. 6, pp. 1–12. Hemisphere, Washington, DC (1978).
3. K. Vafai and M. Sozen, A comparative analysis of multiphase transport model in porous media, *Annual Review of Heat Transfer*, Vol. 3, pp. 145–162. Hemisphere, Washington, DC (1990).
4. Y. Ogniewicz and C. L. Tien, Analysis of condensation in porous insulation, *Int. J. Heat Mass Transfer* **24,** 421–429 (1981).
5. K. Vafai and S. Sarkar, Condensation effects in a fibrous insulation slab, *ASME J. Heat Transfer* **108,** 667–675 (1986).
6. S. Motakef and M. A. El-Masri, Simultaneous heat and mass transfer with phase change in a porous slab, *Int. J. Heat Mass Transfer* **29,** 1503–1512 (1986).
7. A. P. Shapiro and S. Motakef, Unsteady heat and mass

transfer with phase change in a porous slabs: analytical solutions and experimental results, *Int. J. Heat Mass Transfer* **33,** 163–173 (1990).
8. T. W. Tong and C. L. Tien, Radiative heat transfer in fibrous insulations—Part 1: analytical study, *ASME J. Heat Transfer* **105,** 70–75 (1983).
9. R. L. Houston and S. A. Korpela, Heat transfer through fiberglass insulation, *Proceedings of the Seventh International Heat Transfer Conference*, Vol. 2, pp. 499–504. Hemisphere Washington, DC (1982).
10. R. C. Reid and T. K. Sherwood, *The Properties of Gases and Liquids*, McGraw-Hill, New York (1966).